PHYSICAL REVIEW B **96**, 024401 (2017)

Origin of perpendicular magnetic anisotropy in Co/Ni multilayers

M. Arora,[1,*] R. Hübner,[2] D. Suess,[3] B. Heinrich,[1] and E. Girt[1,†]
[1]*Department of Physics, Simon Fraser University, Burnaby, British Columbia V5A 1S6, Canada*
[2]*Institute of Ion Beam Physics and Materials Research, Helmholtz-Zentrum Dresden-Rossendorf, Dresden, Germany*
[3]*Christian Doppler Laboratory of Advanced Magnetic Sensing and Materials, Faculty of Physics, University of Vienna, 1090 Vienna, Austria*

(Received 19 January 2017; revised manuscript received 26 May 2017; published 5 July 2017)

We studied the variation in perpendicular magnetic anisotropy of (111) textured Au/$N \times$ [Co/Ni]/Au films as a function of the number of bilayer repeats N. The ferromagnetic resonance and superconducting quantum interference device magnetometer measurements show that the perpendicular magnetic anisotropy of Co/Ni multilayers first increases with N for $N \leqslant 10$ and then moderately decreases for $N > 10$. The model we propose reveals that the decrease of the anisotropy for $N < 10$ is predominantly due to the reduction in the magnetoelastic and magnetocrystalline anisotropies. A moderate decrease in the perpendicular magnetic anisotropy for $N > 10$ is due to the reduction in the magnetocrystalline and the surface anisotropies. To calculate the contribution of magnetoelastic anisotropy in the Co/Ni multilayers, in-plane and out-of-plane x-ray diffraction measurements are performed to determine the spacing between Co/Ni (111) and (220) planes. The magnetocrystalline bulk anisotropy is estimated from the difference in the perpendicular and parallel g factors of Co/Ni multilayers that are measured using the in-plane and out-of-plane ferromagnetic resonance measurements. Transmission electron microscopy has been used to estimate the multilayer film roughness. These values are used to calculate the roughness-induced surface and magnetocrystalline anisotropy coefficients as a function of N.

DOI: 10.1103/PhysRevB.96.024401

I. INTRODUCTION

Co/Ni multilayers (MLs) exhibit high spin polarization [1], large perpendicular magnetic anisotropy (PMA) [2–6], and low intrinsic damping [7–10] that make them a promising candidate for the spintronic devices such as spin-transfer torque random access memory (STT-RAM) [11], spin-torque oscillators [12], and bit patterned media [13–18].

Daalderop *et al.* [3] predicted and experimentally demonstrated the PMA in (111) oriented Co(1 AL)/Ni(2 AL) MLs (AL—atomic layer) in 1992. The calculations by Daalderop *et al.* [3] suggested that the PMA arises from the reduced symmetry and electronic structure at Co and Ni interfaces. They emphasized that in Co(1 AL)/Ni(2 AL) MLs the Fermi energy is close to the bands with d_{xy} and $d_{x^2-y^2}$ characters (z axis is chosen to be normal to the interface) whose spin-orbit interaction favors the PMA. Calculations by Kyuno *et al.* [19] also attributed the origin of PMA in (111) Co/Ni MLs to large local density of states of $d_{x^2-y^2}$ and d_{xy} orbitals of Co and Ni minority spin just below the Fermi energy. PMA is also observed in (100) and (110) oriented Co/Ni MLs [20]. Some groups also pointed out that the magnetoelastic anisotropy due to strain in Co/Ni MLs is a source of PMA [21–24]. Since these initial studies, many authors [2,5,6,20–26] have studied the anisotropy in Co/Ni ML, however, the origin of the PMA in these MLs is still a matter of debate.

Several authors have studied PMA in Co/Ni MLs as a function of the Co and Ni layer thicknesses [2,5,6,20,25,27,28]. They found that the maximum PMA can be achieved for the Co layer thickness between 1 and 2 ALs and for the Ni layer thickness around 3 ALs. Growth conditions, choice of a substrate, and seed layers play an important role to improve the (111) texture and hence the PMA of Co/Ni MLs [27–30]. Postdeposition techniques such as annealing [30–32] and ion irradiation [33] were also studied to tune the PMA in Co/Ni MLs.

Co/Ni MLs became a model system for spin-transfer torque studies in the perpendicularly magnetized magnetic materials due to their large and tunable PMA and a relatively low damping constant α. One way to tune the magnetic characteristics of these MLs is by varying the number of bilayer repeats N. However, reports on the behavior of the magnetic anisotropy as a function of N have varied in the literature [8,34–45] and they exhibit strong dependence on the layers adjacent to the Co/Ni MLs.

In this paper, we investigated the influence of Au interface layers on the magnetic anisotropy of Co/Ni MLs. We studied the magnetic anisotropy of as-deposited and annealed Co(0.21)/Ni(0.58) MLs (thicknesses in nm) as a function of the number of MLs, N. For these Co and Ni film thicknesses the Co/Ni MLs have the largest perpendicular magnetic anisotropy [2]. We modeled the observed anisotropy variations by taking into account the contributions from (1) the magnetoelastic anisotropy due to the strain, (2) the magnetocrystalline anisotropy due to the orbital asymmetry between the easy and hard axes, (3) the roughness-induced anisotropies, and (4) the interdiffusion of Au in the Co/Ni MLs.

II. THEORY

To understand the dependence of magnetic anisotropy of the Co/Ni MLs on the number of multilayers, the total energy density of the MLs will be expressed as

$$e_{\text{tot}} = -(K_u + K_{\text{DIP}})\cos^2\theta, \tag{1}$$

where K_u is the total intrinsic magnetic anisotropy given as

$$K_u = K_{\text{ME}} + K_{\text{MC}} + K_S/d. \tag{2}$$

---

[*] mmonika@sfu.ca

[†] egirt@sfu.ca

©2017 American Physical Society

K_{ME}, K_{MC}, K_{DIP}, and K_S are the magnetoelastic, magnetocrystalline, dipolar, and surface anisotropy coefficients, respectively. θ is the angle between the normal to the film and the magnetization, and d is the thickness of the Co/Ni MLs. The contribution to the magnetic anisotropy energy due to diffusion of Au in the Co/Ni MLs will be discussed only qualitatively.

A. Magnetoelastic anisotropy, K_{ME}

Co ($a_{\mathrm{Co},fcc} = 0.354$ nm) [46] and Ni ($a_{\mathrm{Ni},fcc} = 0.352$ nm) [47] are closely lattice matched. The Au interplanar distance ($a_{\mathrm{Au},fcc} = 0.408$ nm) is about 14% larger than that of Co and Ni that causes strain in the Co/Ni MLs. To understand the effect of strain on the magnetic anisotropy of the Co/Ni MLs, we estimated the strain-induced bulk magnetoelastic energy per volume for all the multilayer samples. The magnetoelastic anisotropy coefficient for the cubic (111) structures is estimated as [21,48]

$$K_{\mathrm{ME}} = \frac{B_2^{\mathrm{Ni}}(\epsilon_{\parallel} - \epsilon_{\perp})_{\mathrm{Ni}} V_{\mathrm{Ni}}}{V_{\mathrm{Ni}} + V_{\mathrm{Co}}} + \frac{B_2^{\mathrm{Co}}(\epsilon_{\parallel} - \epsilon_{\perp})_{\mathrm{Co}} V_{\mathrm{Co}}}{V_{\mathrm{Ni}} + V_{\mathrm{Co}}}, \tag{3}$$

where $B_2^{\mathrm{Ni}}(\mathrm{fcc}) = 10\ \mathrm{MJ/m^3}$, $B_2^{\mathrm{Co}}(\mathrm{fcc}) = 7.7\ \mathrm{MJ/m^3}$, and $\epsilon_{\parallel}$ and $\epsilon_{\perp}$ are the in-plane and out-of-plane strains, respectively. $\epsilon_{\parallel,\perp}$ are calculated as $\epsilon_{\parallel} = [d(220)_{st} - d(220)_{ust}]/d(220)_{ust}$ and $\epsilon_{\perp} = [d(111)_{st} - d(111)_{ust}]/d(111)_{ust}$, where $d(220)_{st}$ and $d(220)_{ust}$ are the distances between (220) planes of strained and unstrained Co/Ni MLs, respectively, and $d(111)_{st}$ and $d(111)_{ust}$ are the distances between (111) planes of the strained and unstrained Co/Ni MLs, respectively. In the studied Co(0.21)/Ni(0.58) MLs, $V_{\mathrm{Co}}/(V_{\mathrm{Ni}} + V_{\mathrm{Co}}) = 0.25$ and $V_{\mathrm{Ni}}/(V_{\mathrm{Ni}} + V_{\mathrm{Co}}) = 0.75$. In these calculations we assumed that the Co/Ni MLs have a fcc structure. This is in agreement with the scanning transmission electron microscopy (STEM) results of Gottwald *et al.* [4] that showed A-B-C stacking of the (111) planes in the (111) textured $\mathrm{Co_{1ML}/Ni_{3ML}}$ [$\approx$Co(0.21)/Ni(0.58) ML]. In-plane and out-of-plane x-ray diffraction (XRD) measurements are used to measure $d(220)_{st}$ and $d(111)_{st}$, respectively, in order to calculate the $\epsilon_{\parallel}$ and $\epsilon_{\perp}$.

B. Magnetocrystalline anisotropy, K_{MC}

According to Bruno's theory the magnetocrystalline anisotropy coefficient of the Co/Ni MLs per volume, K_{MC}, originates from the asymmetry in the orbital moment between the hard and easy axes and can be written as [49,50]

$$K_{\mathrm{MC}} = \left(\alpha \frac{n\xi}{4V}\right) \frac{\Delta\mu_L}{\mu_B}, \tag{4}$$

where ξ is the spin-orbit coupling parameter, α is the prefactor that varies between 0 and 0.2 and is a function of electronic structure, n is the number of atoms per unit cell, V is the volume of the unit cell, μ_B is the Bohr magneton, and $\Delta\mu_L$ is the difference in orbital moments between the easy and hard magnetization axes [50,51]. The orbital moment is proportional to the g factor, g, that can be determined from the ferromagnetic resonance (FMR) measurements. For films the orbital asymmetry is given by [51]

$$\Delta\mu_L = \frac{\mu_s}{2}(g^{\perp} - g^{\parallel}), \tag{5}$$

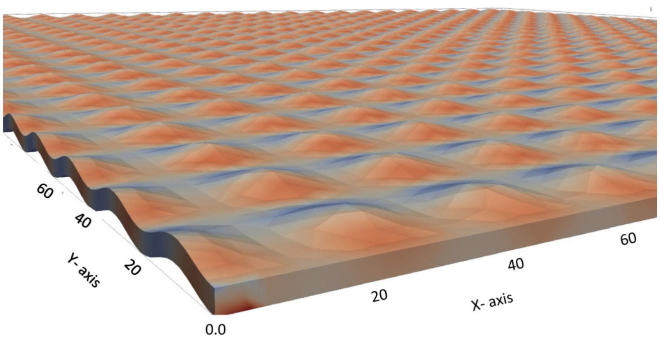

FIG. 1. Simulated ML roughness used for the numerical calculation of the total dipolar surface anisotropy coefficient, $K_S^{\mathrm{DIP}}(\mathrm{calc})$.

where μ_s is the spin magnetic moment and can be determined from the ratio of $\mu_L/\mu_s = (g-2)/2$ and the total magnetic moment $\mu = \mu_s + \mu_L$, and $g^{\perp}$ and $g^{\parallel}$ are the out-of-plane and in-plane g factors, respectively. Superconducting quantum interference device (SQUID) magnetometer measurements are used to calculate μ_s, where $\mu_s = 2M_s/(ng)$, M_s is the saturation magnetization of the Co/Ni MLs, and n is the number of atoms per unit volume.

C. Dipolar magnetic anisotropy including surface roughness, K_{DIP}

The dipolar anisotropy coefficient can be expressed as

$$K_{\mathrm{DIP}} = K_V^{\mathrm{DIP}} + K_S^{\mathrm{DIP}}/d, \tag{6}$$

where $K_V^{\mathrm{DIP}} = -\mu_0 M_s^2/2$ is the dipolar volume anisotropy coefficient of perfectly flat films, and d is ML thickness. If the roughness of the top and bottom surfaces is uncorrelated the dipolar surface anisotropy coefficient, K_S^{DIP}, can be calculated analytically as $K_S^{\mathrm{DIP}} = K_{S,T}^{\mathrm{DIP}} + K_{S,B}^{\mathrm{DIP}}$, where [52]

$$K_{S,T,B}^{\mathrm{DIP}} = \mu_0 M_s^2 \tfrac{3}{8} \sigma_{T,B}\{1 - f[2\pi(\sigma_{T,B}/\xi_{T,B})]\}. \tag{7}$$

Here $K_{S,T}^{\mathrm{DIP}}$ and $K_{S,B}^{\mathrm{DIP}}$ are the dipole surface anisotropy coefficients of the top and bottom interfaces, respectively. $\sigma_{T,B}$ is the mean deviation of the top and bottom ML surfaces from an ideally flat surface, $\xi_{T,B}$ is an average lateral size of the terraces at the top and bottom ML surfaces, and f is the function calculated by Bruno [52]. In our calculations of K_S^{DIP} in Ta/Au/$N \times$[Co/Ni]/Au films, we will assume that $\sigma_B = \sigma^{\mathrm{Au/Co}}$ and $\sigma_T = \sigma^{\mathrm{Ni/Au}}$ are the roughnesses of the bottom and top surfaces of the Co/Ni MLs, respectively, and $\xi_B = \xi^{\mathrm{Au/Co}}$ and $\xi_T = \xi^{\mathrm{Ni/Au}}$ are the roughness periods of the bottom and top surfaces of the Co/Ni MLs, respectively.

Since the roughness of the top and bottom surfaces in the ML is nearly correlated, we also calculated $K_S^{\mathrm{DIP}}(\mathrm{calc})$ numerically. The calculations were done for films with the correlated roughness of the top and bottom surfaces as shown in Fig. 1. The numeric calculation will be used to determine the reduction of the anisotropy in the ML due to roughness. We also performed numerical calculations assuming that the top surface is rough and the bottom surface is flat. We will show later that $K_{S,r-f}^{\mathrm{DIP}}(\mathrm{calc})$ of a film with the rough top and the flat bottom surfaces is similar to that of a film with two correlated rough surfaces.

TABLE I. N, d, σ, and ξ are the number, thicknesses, roughness, and roughness period of the Co/Ni MLs, respectively. For $N = 0$, $\sigma = \sigma^{\mathrm{Au/Co}}$ and $\xi = \xi^{\mathrm{Au/Co}}$ are the roughness and roughness period of the bottom Co/Ni ML surface (Au/ML interface). For $N > 0$, $\sigma = \sigma^{\mathrm{Ni/Au}}$ and $\xi = \xi^{\mathrm{Ni/Au}}$ are the roughness and roughness period of the top Co/Ni ML surface (ML/Au interface). $K_V^{\mathrm{DIP}} = -\mu_0 M_s^2/2$ is the dipolar volume anisotropy coefficient of a perfectly flat ML, $K_S^{\mathrm{DIP}} = K_{S,T}^{\mathrm{DIP}} + K_{S,B}^{\mathrm{DIP}}$, where $K_{S,T}^{\mathrm{DIP}}$ and $K_{S,B}^{\mathrm{DIP}}$ are calculated using Eq. (7), $K_{\mathrm{DIP}} = K_V^{\mathrm{DIP}} - K_S^{\mathrm{DIP}}/d$, and $H_{\mathrm{DIP}} = 2K_{\mathrm{DIP}}/\mu_0 M_s$. K_{DIP}(calc) and H_{DIP}(calc) are the total dipolar anisotropy coefficient and field of rough ML calculated using numerical methods.

N	d (nm)	ξ (nm)	σ (nm)	K_V^{DIP} (10^5 J/m^3)	K_S^{DIP}/d (10^4 J/m^3)	K_{DIP} (10^5 J/m^3)	H_{DIP} (10^5 A/m)	K_S^{DIP}/d(calc) (10^4 J/m^3)	K_{DIP}(calc) (10^5 J/m^3)	H_{DIP}(calc) (10^5 A/m)
0		22.5	0.80							
4	3.2	23.0	1.20	−2.26	3.13	−1.95	−5.17	0.62	−2.20	−5.83
6	4.8	23.3	1.32	−2.96	3.02	−2.65	−6.16	0.86	−2.87	−6.66
8	6.4	23.6	1.40	−3.11	2.49	−2.86	−6.47	0.83	−3.02	−6.84
10	8.0	23.8	1.46	−3.62	2.45	−3.37	−7.08	0.89	−3.53	−7.40
16	12.8	24.5	1.60	−3.62	1.70	−3.45	−7.23	0.73	−3.55	−7.44
32	25.6	26.0	1.80	−3.62	0.96	−3.52	−7.39	0.44	−3.58	−7.50
64	51.2	27.5	2.00	−3.41	0.50	−3.36	−7.26	0.25	−3.39	−7.32

In order to calculate the effective shape anisotropy finite element simulations are performed. The topography of the top surface as a function of the x and y coordinates is generated according to the following function:

$$Z(x,y) = 2\sigma \cos^2\left(\frac{2\pi x}{\lambda}\right)\sin^2\left(\frac{2\pi y}{\lambda}\right), \tag{8}$$

where the wavelength is $\lambda = 2\xi$. The parameters ξ and σ are given in Table I. Two different geometries are calculated. The first geometry is calculated by extruding the top and bottom surfaces according to Eq. (8). Hence, the thickness d, which is along the z direction, is independent of the position x,y. For the second geometry we consider that the bottom surface is flat and the top surface has roughness of the form given by the function $Z(x,y)$ [see Eq. (8)]. The average thickness of the film is the same and equals d. The dimension in x and y direction is 500 nm × 500 nm. The obtained volume is discretized in tetrahedral finite elements with mesh size of 4 nm.

In order to calculate the stray field for a given magnetization which points either in the direction (001) or (010) the hybrid finite element/boundary element method is employed [53] using a magnetic scalar potential. The open boundary problem is accurately solved by the boundary element method, which effectively transforms the boundary condition of vanishing potential at infinity to the boundary of the magnet. The magnetostatic energy is calculated for the out-of-plane magnetization, $E_\perp$, and in-plane magnetization, $E_\parallel$. The effective shape anisotropy is calculated as

$$K_{\mathrm{DIP}}(\mathrm{calc}) = \frac{1}{V}(E_\parallel - E_\perp). \tag{9}$$

In order to correct for the finite size of the simulated structure, we also evaluated Eq. (9) for the corresponding film without surface roughness but for the same lateral dimensions and thickness, denoted by K_V^{DIP}. The effective anisotropy due to surface roughness can be approximated by

$$K_S^{\mathrm{DIP}}(\mathrm{calc})/d = K_{\mathrm{DIP}}(\mathrm{calc}) - K_V^{\mathrm{DIP}}, \tag{10}$$

which is not dependent on the lateral dimension of the simulated film in the first order.

From K_{DIP} [Eq. (6)] and K_{DIP}(calc) [Eq. (9)] one can calculate the average demagnetization fields, H_{DIP} and H_{DIP}(calc), respectively, in the films along the direction perpendicular to the film surface using formula

$$H = -\frac{1}{\mu_0}\frac{2K_{\mathrm{DIP}}}{M_s}. \tag{11}$$

D. Surface anisotropy, K_S

The surface anisotropy arises from the fact that surface atoms have an asymmetric environment as compared with bulk atoms. The total surface anisotropy coefficient of our Ta/Au/N × [Co/Ni]/Au ML is given by

$$\frac{K_S}{d} = \frac{\left(K_S^{\mathrm{Au/Co}} + K_S^{\mathrm{Ni/Au}}\right)}{N t_{\mathrm{BL}}} + \frac{(2N-1)}{N t_{\mathrm{BL}}} K_S^{\mathrm{Co/Ni}}, \tag{12}$$

where $K_S^{\mathrm{Au/Co}}$, $K_S^{\mathrm{Ni/Au}}$, and $K_S^{\mathrm{Co/Ni}}$ are the surface magnetocrystalline anisotropy coefficients at Au/Co (the bottom interface between Au and the Co/Ni ML), Ni/Au (the top interface between the Co/Ni ML and Au), and Co/Ni interfaces, respectively. In Eq. (12) we assumed that the Co/Ni and Ni/Co interface anisotropies are the same. The ML thickness $d = N t_{\mathrm{BL}}$, where N is number of multilayers and $t_{\mathrm{BL}} = t_{\mathrm{Co}} + t_{\mathrm{Ni}}$ is the thickness of the Co/Ni bilayer.

In rough films, some in-plane magnetic atoms are missing at the surface, which reduces the asymmetry character of the surface atoms. In our Ta/Au/N × [Co/Ni]/Au ML this causes a reduction in the magnetocrystalline surface anisotropy coefficients, $K_S^{\mathrm{Au/Co}}$, $K_S^{\mathrm{Ni/Au}}$, and $K_S^{\mathrm{Co/Ni}}$. This effect has been calculated by Bruno [54] and for the Au/Co and Ni/Au interfaces can be calculated as

$$\Delta K_S^{\mathrm{Au/Co}} = -2K_S^{\mathrm{Au/Co}} \frac{\sigma^{\mathrm{Au/Co}}}{\xi^{\mathrm{Au/Co}}}, \tag{13}$$

$$\Delta K_S^{\mathrm{Ni/Au}} = -2K_S^{\mathrm{Ni/Au}} \frac{\sigma^{\mathrm{Ni/Au}}}{\xi^{\mathrm{Ni/Au}}}, \tag{14}$$

where $\sigma^{\mathrm{Au/Co}}$ and $\sigma^{\mathrm{Ni/Au}}$ are the film surface roughnesses, and $\xi^{\mathrm{Au/Co}}$ and $\xi^{\mathrm{Ni/Au}}$ are the film surface roughness periods at the bottom and top interfaces of the Co/Ni MLs with Au.

In addition, roughness will also affect the magnetocrystalline surface anisotropy coefficient at Co/Ni interfaces across the ML. This can be calculated as

$$\Delta K_S^{\mathrm{Co/Ni}} = -\frac{2K_S^{\mathrm{Co/Ni}}}{2N-1}\sum_{i=1}^{2N-1}\frac{\sigma_i^{\mathrm{Co/Ni}}}{\xi_i^{\mathrm{Co/Ni}}}, \tag{15}$$

where $\sigma_i^{\mathrm{Co/Ni}}$ and $\xi_i^{\mathrm{Co/Ni}}$ are the roughness and roughness period of the ith Co/Ni interface of the MLs, respectively.

Thus, to include the magnetocrystalline surface anisotropy that arises from the roughness of our MLs, $K_S^{\mathrm{Au/Co}}$, $K_S^{\mathrm{Ni/Au}}$, and $K_S^{\mathrm{Co/Ni}}$ in Eq. (12) have to be substituted with $K_S^{\mathrm{Au/Co}} + \Delta K_S^{\mathrm{Au/Co}}$, $K_S^{\mathrm{Ni/Au}} + \Delta K_S^{\mathrm{Ni/Au}}$, and $K_S^{\mathrm{Co/Ni}} + \Delta K_S^{\mathrm{Co/Ni}}$, respectively.

E. Interdiffusion-induced anisotropy energy

Another source of anisotropy could also be due to the interdiffusion of Au into the Co/Ni ML. According to Néel's model, diffusion of Au in the Co/Ni ML will introduce randomness in the magnetic pair bonds, which will reduce the interface anisotropy [55]. This is in agreement with the calculations by Draaisma and de Jonge [56]. They show that the magnetic anisotropy from the pair interaction strongly decreases with the increase of the degree of mixing. Broeder *et al.* [57] used ion-beam sputtering to deposit Au/Co MLs. The MLs had rather diffuse interfaces due to the Ar-ion bombardment during the growth. To expel Au from Co layers the MLs were annealed up to 300 °C resulting in a strong increase of the interface anisotropy, enhanced PMA. This increase in PMA was accompanied by a strong increase of the intensity of the multilayer reflections observed in XRD experiments, and was interpreted as a sharpening of the Co/Au interfaces.

Since interdiffusion is the most pronounced at the interface we expect that the reduction of PMA will scale with the film thickness. In the Co/Ni MLs the contribution to anisotropy due to interdiffusion will decrease with the number of multilayers. In this paper we will use element mapping based on energy-dispersive x-ray spectroscopy (EDXS) in transmission electron microscopy (TEM) to detect the interdiffusion of Au in the Co/Ni MLs. We will show that the Au concentration in the Co/Ni MLs can be reduced by postdeposition annealing of the MLs. Comparing magnetic properties of the Co/Ni MLs before and after annealing will help us understand how the Au interdiffusion impacts the magnetic anisotropy of the MLs.

III. EXPERIMENT

Ta(3)/Au(12)/$N\times$[Co(0.21)/Ni(0.58)]/Au(12) films were deposited at room temperature on Si(100) wafers by means of magnetron sputtering, where the numbers in parentheses indicate the layer thicknesses in nanometers, and $N = 4$, 6, 8, 10, 16, 32, and 64 is the number of bilayer repeats. These multilayer samples were also annealed at 523 and 553 K for 1 h to study the postannealing effects. The base pressure of the deposition system was below 5×10^{-8} Torr and a sputter process was performed at an Ar pressure of 2×10^{-3} Torr. Before deposition, the substrates were cleaned with hexane and methanol under ultrasonic conditions at 333 K. The substrates were also heated to 523 K in vacuum in the sputter system for 10 mins to remove any adsorbed layers. Low-angle x-ray reflectivity measurements were used to extract the film thicknesses. We also used a thickness monitor to measure the thicknesses of the sputtered films.

The distances between lattice planes parallel and perpendicular to the film surfaces were measured with in-plane and out-of-plane XRD measurements, respectively. In both cases, we used a Cu $K\alpha$ radiation source. For the in-plane XRD measurements, the incident and scattered beams are nearly parallel to the sample surface. This allows the measurements of spacing between lattice planes nearly perpendicular to the sample surface. In-plane XRD measurements were performed at a grazing angle of 0.65°. Out-of-plane XRD measurements were performed with the scattering wave vector normal to the film surface. We used Gaussian functions to fit the in-plane and out-of-plane XRD peaks and find the peak positions. XRD data indicate that all the Co/Ni multilayers have (111) texture with the full width at half maximum of the c-axis distribution below 3°.

Bright-field and high-angle annular dark-field STEM imaging as well as element mapping based on EDXS were performed at 200 kV with a Talos F200X microscope equipped with a Super-X EDXS detector system (FEI). Prior to TEM analysis, the specimen mounted in a high-visibility low-background holder was placed for 10 s into a Model 1020 Plasma Cleaner (Fischione) to remove organic contamination.

The field dependence of the magnetization is measured using a SQUID magnetometer. The measurements are performed in magnetic fields up to 5.5×10^6 A/m (70 kOe) and with the field direction parallel and perpendicular to the sample surface. K_u(SQUID) is calculated by finding the area enclosed between the hard and easy axes M(H) curves and by adding to this area K_{DIP}(calc) calculated using Eq. (9) [55]. SQUID measurements of $8\times$[Co/Ni] multilayers along the hard and easy axes at 298 and 5 K are shown in the Supplemental Material [58]. The numerically calculated values of K_{DIP}(calc) as a function of N are listed in Table I.

FMR measurements were carried out at room temperature using a terminated waveguide over the frequency range from 45 to 70 GHz. Field modulation and lock-in techniques were used to obtain the conventional field derivative of the sample absorption. The fitting procedure of FMR data was described by Montoya *et al.* [59,60]. Field was applied in the parallel and perpendicular directions to the film plane to measure effective fields $\mu_0 M_{\mathrm{eff}}$ and g factors for both the hard and easy axes. For the in-plane and perpendicular geometry of the FMR setup, the resonance conditions are respectively given by

$$\begin{aligned}\left(\frac{\omega}{\gamma_\parallel}\right)^2 &= \mu_0^2 H_{\mathrm{FMR}}\left(H_{\mathrm{FMR}} + M_{\mathrm{eff}}^{\parallel}\right),\\ \frac{\omega}{\gamma_\perp} &= \mu_0\left(H_{\mathrm{FMR}} - M_{\mathrm{eff}}^{\perp}\right),\end{aligned} \tag{16}$$

where $\gamma_\parallel = g_\parallel \mu_B/\hbar$ and $\gamma_\perp = g_\perp \mu_B/\hbar$ are the parallel and perpendicular to the film surface gyromagnetic ratios, and H_{FMR} is the resonance field. Plots of resonance field versus frequency of $8\times$[Co/Ni] multilayers obtained from FMR measurements with the applied field parallel and perpendicular to the sample surface are shown in the Supplemental Material

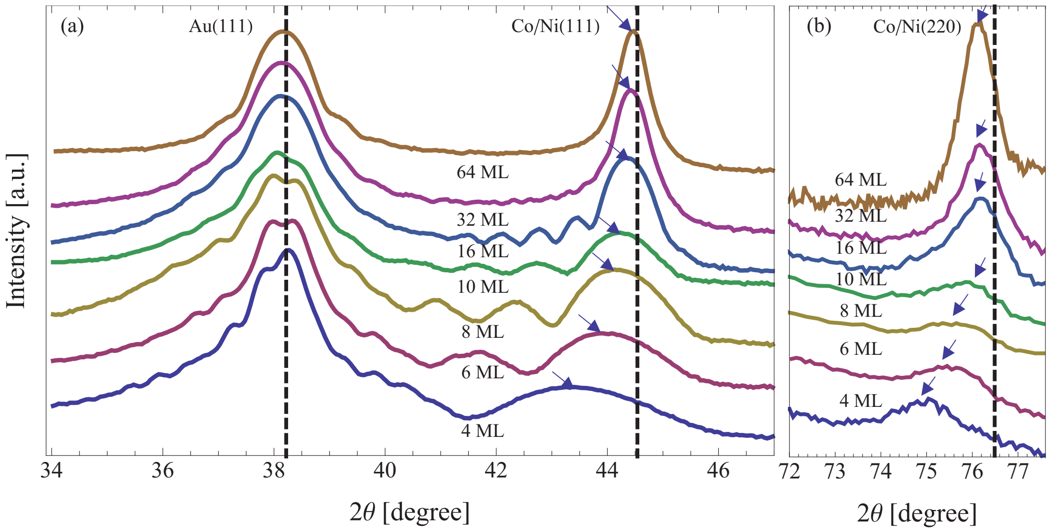

FIG. 2. (a) Out-of-plane and (b) in-plane x-ray measurements of as-deposited Ta(3)/Au(12)/$N\times$[Co(0.21)/Ni(0.58)]/Au(12) with $N = 4$, 6, 8, 10, 16, and 32. The dashed lines at 38.22°, 44.54°, and 76.49° represent the expected positions of unstrained Au (111), $N \times$ [Co/Ni] (111) and $N \times$ [Co/Ni] (220) peaks, respectively. The arrows indicate the fitted positions of the $N \times$ [Co/Ni] (111) and (220) peaks. We assumed that the Co/Ni MLs have fcc structure in agreement with STEM results by Gottwald *et al.* [4].

[58]. The effective magnetic fields parallel and perpendicular to the film surface are given by

$$M_{\text{eff}}^{\parallel} = M_s^{\parallel} - \frac{2K_2^{\perp}}{\mu_0 M_s^{\perp}},$$
$$M_{\text{eff}}^{\perp} = M_s^{\perp} - \frac{2K_2^{\perp}}{\mu_0 M_s^{\perp}} - \frac{2K_4^{\perp}}{\mu_0 M_s^{\perp}}, \tag{17}$$

where $g_{\parallel}$, $M_s^{\parallel}$, and $M_{\text{eff}}^{\parallel}$ are the in-plane g factor, saturation magnetization, and effective magnetization, respectively, and $g_{\perp}$, $M_s^{\perp}$, and $M_{\text{eff}}^{\perp}$ are the perpendicular to plane g factor, saturation magnetization, and effective magnetization, respectively. $K_2^{\perp}$ and $K_4^{\perp}$ are the second- and fourth-order constants of the magnetic uniaxial anisotropy. Equation (17) has been derived by assuming that the definition of the anisotropy energy density is $e = \mu_0 M_s^2/2\cos^2\theta - K_2^{\perp}\cos^2\theta - K_4^{\perp}/2\cos^4\theta$, and that the investigated magnetic films are polycrystalline, textured, and have no in-plane anisotropy.

To account for the reduction in the dipole anisotropy due to the ML roughness Eq. (17) is modified as

$$M_{\text{eff}}^{\parallel} = M_{s,\text{corr}}^{\parallel} - \frac{2K_2^{\perp}}{\mu_0 M_s^{\perp}},$$
$$M_{\text{eff}}^{\perp} = M_{s,\text{corr}}^{\perp} - \frac{2K_2^{\perp}}{\mu_0 M_s^{\perp}} - \frac{2K_4^{\perp}}{\mu_0 M_s^{\perp}}, \tag{18}$$

where $M_{s,\text{corr}}^{\parallel} = M_s^{\parallel} - 2K_S^{\text{DIP}}/(M_s d)$ and $M_{s,\text{corr}}^{\perp} = M_s^{\perp} - 2K_S^{\text{DIP}}/(M_s d)$ are the in-plane and perpendicular to the plane saturation magnetizations corrected for the ML roughness, respectively. The dipolar surface anisotropy coefficients, due to the ML roughness, are calculated numerically, $K_S^{\text{DIP}} = K_S^{\text{DIP}}(\text{calc})$, and are listed in Table I. We will assume that the saturation magnetization is independent of the direction of magnetic field $M_s^{\perp} = M_s^{\parallel}$. This is a good approximation since $(g^{\perp} - g^{\parallel})/g^{\parallel} < 1\%$.

IV. RESULTS AND DISCUSSION

A. As-deposited films

1. X-ray measurements

Figures 2(a) and 2(b) represent the out-of-plane and in-plane x-ray diffraction measurements, respectively, of Ta(3)/Au(12)/$N\times$[Co(0.21)/Ni(0.58)]/Au(12) with $N = 4$, 6, 8, 10, 16, 32, and 64. The out-of-plane x-ray measurements, Fig. 2(a), show two major Bragg peaks that correspond to Au(111) and Co/Ni(111) planes. The dashed black lines at 38.22° and 44.54° represent the expected positions of Au and Co/Ni(111) peaks, respectively, in the unstrained lattices. The position of the Co/Ni(111) peak shifts from 44.42° to 43.40° with the change of N from 64 to 4. This shows that the spacing between the (111) planes, $d_{(111)}$, in the Co/Ni MLs increases with decreasing N. The change in spacing between Co/Ni(111) planes as a function of N is shown in Fig. 3(a) (left axis). The presence of thickness fringes is seen on both sides of the two primary peaks of Au(111) and Co/Ni(111) [see Fig. 1(a)]. We also obtained the thickness of $N\times$[Co(0.21)/Ni(0.58)] from the period of oscillation of the thickness fringes. The calculated thicknesses are the same as measured by the thickness monitor.

The dashed line at 76.49° [see Fig. 2(b)] represents the expected position of the unstrained Co/Ni(220) peak. For $N = 64$, the Co/Ni(220) peak is shifted to 76.22°. With decreasing N, the Co/Ni(220) peak further shifts to lower angles, which indicates an increase in spacing between the (220) lattice planes, $d_{(220)}$. This change in the lattice spacing as a function of N is shown in Fig. 3(a) (right axis). This behavior is expected since the distance between the (220) planes in Au is 14% larger than the distance between the (220) planes of the Co/Ni MLs.

In a strained film, it is assumed that the volume/atom of the film remains constant [61]. Therefore, it is expected that if there is lattice expansion along one direction, there should be

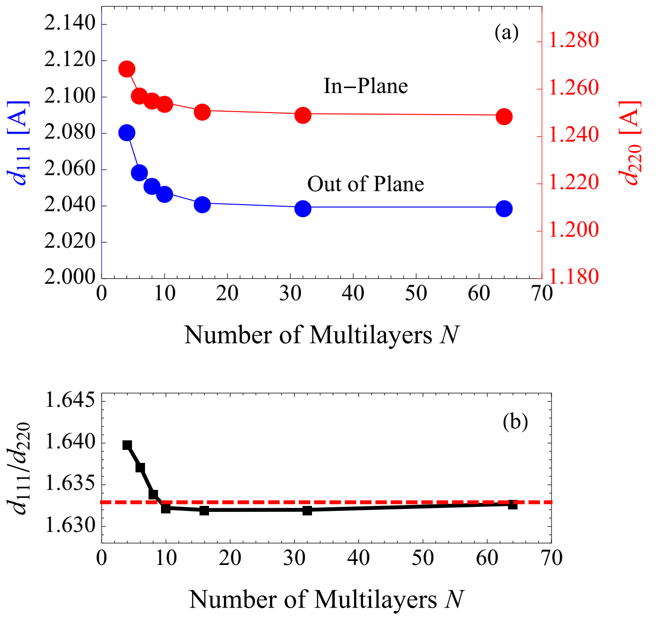

FIG. 3. (a) The spacing between the (111) ($d_{(111)}$) and (220) ($d_{(220)}$) lattice planes and (b) $d_{(111)}/d_{(220)}$ of the as-deposited Co/Ni MLs as a function of N. The dashed red line represents the expected $d_{(111)}/d_{(220)}$ for the ideal cubic lattice structure. The x-ray measurements are performed at room temperature.

lattice contraction in the perpendicular direction. However, in the present case, with the decrease in the number of MLs, the spacings between both the Co/Ni(111) planes parallel to the film surface and the Co/Ni(220) planes orthogonal to the film surface increase. Diffusion of Au atoms into the Co/Ni MLs associated with lattice expansion of the latter ones could be an explanation for the observed behavior, as shown in the next section.

The ratio $d_{(111)}/d_{(220)}$ of the as-deposited Co/Ni MLs is plotted as a function of N in Fig. 3(b). From Fig. 3(b) it is evident that $d_{(111)}/d_{(220)}$ decreases with N for $N \leqslant 10$. For $N \geqslant 16$, $d_{(111)}/d_{(220)}$ gradually increases, approaching the ideal cubic crystal $d_{(111)}/d_{(220)}$ ratio for $N = 64$. The observed tetragonal distortion of the Co/Ni ML lattice for $N \leqslant 10$ can have a profound effect on the intrinsic magnetic properties such as inducing difference in orbital moments between [111] and [220] crystal directions.

2. *Microstructure of Co/Ni ML*

To analyze the element distribution, EDXS analyses were performed in STEM mode for the Co/Ni ML samples with $N = 16$ and 32. In particular, Fig. 4(a) shows a cross-sectional bright-field STEM image of Ta(3)/Au(12)/$N\times$[Co(0.21)/Ni(0.58)]/Au(12), and Figs. 4(b)–4(d) present the corresponding Au, Ni, and Co element maps, respectively. According to Fig. 4(b), some gold is detected within the Co/Ni MLs with a higher Au concentration close to the bottom Au/[Co/Ni] interface. Such gold diffusion into the ML stack might explain the Co/Ni ML lattice expansion observed in the x-ray diffraction measurements. Additionally, Figs. 4(c) and 4(d) show the presence of Co and Ni within both top and bottom gold layers, in particular along Au grain boundaries. It should be mentioned, however, that small Co and Ni background signals within both Au layers can be due to fluorescence excitation triggered by higher-energy Au x rays. There is also some Co and Ni at the top of the film stack. This can be explained by a small amount of Co and Ni that effectively floats on the surface during Au deposition.

Figures 5(a) and 5(b) are cross-sectional bright-field overview STEM images of Ta(3)/Au(12)/16×[Co(0.21)/Ni(0.58)]/Au(12) (16 ML) and Ta(3)/Au(12)/32×[Co(0.21)/Ni(0.58)]/Au(12) (32 ML), respectively. For both samples, the Co/Ni MLs were grown on top of a Au seed layer which is characterized by an average Au grain size (average roughness period) of $\xi = \xi^{\mathrm{Au/Co}} = 21$ nm. Regarding the top ML/Au interface, the average roughness period, $\xi = \xi^{\mathrm{Ni/Au}}$, is 23 nm for the 16 ML and 25 nm for the 32 ML sample, respectively. The average roughness (i.e., the mean deviation

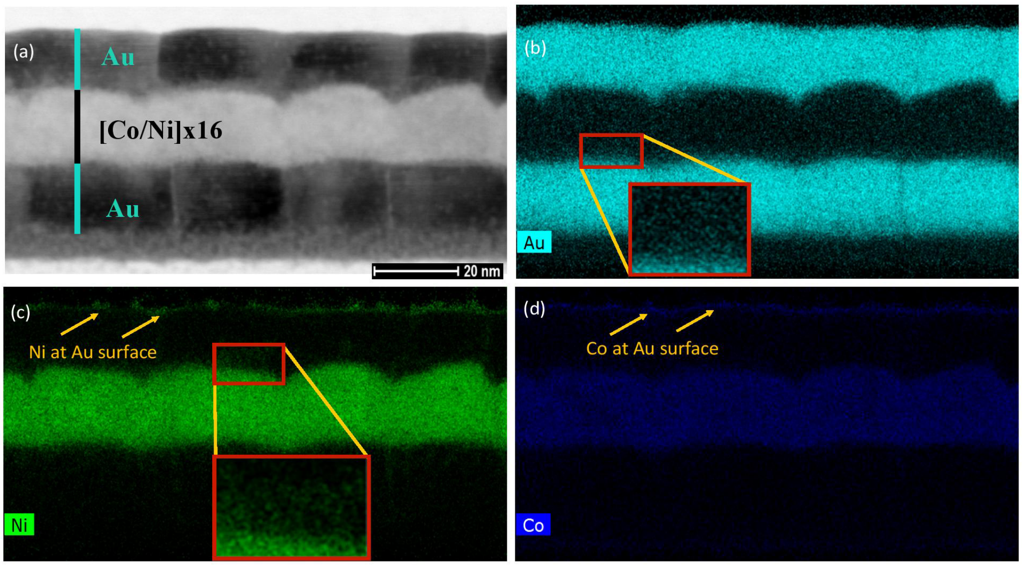

FIG. 4. (a) Cross-sectional bright-field STEM micrograph of Ta(3)/Au(12)/16×[Co(0.21)/Ni(0.58)]/Au(12) (b) with corresponding element maps for Au (c) for Ni and (d) for Co obtained by EDXS analysis.

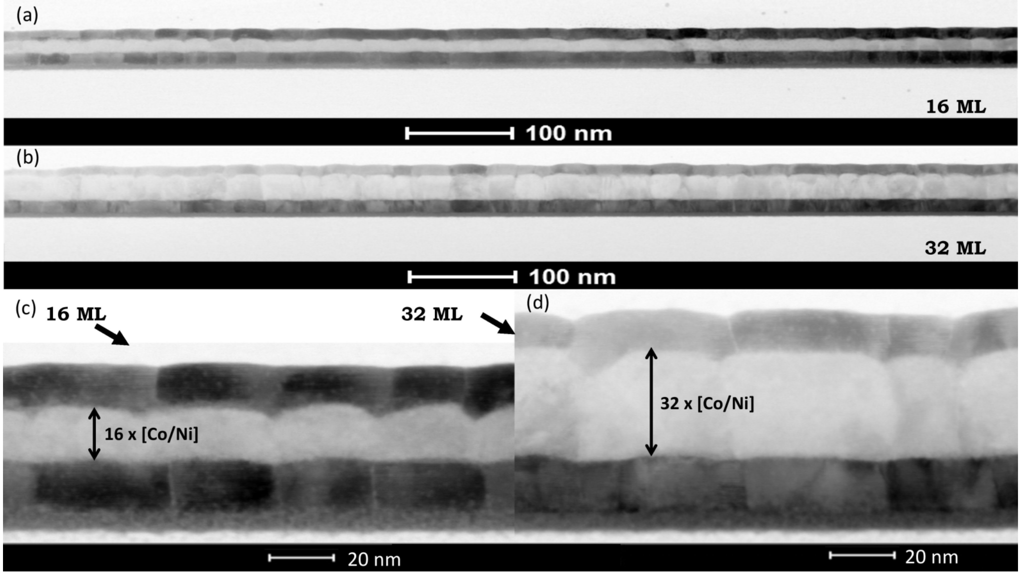

FIG. 5. Cross-sectional bright-field STEM micrographs of Ta(3)/Au(12)/16×[Co(0.21)/Ni(0.58)]/Au(12) (a) and (c), and of Ta(3)/Au(12)/32×[Co(0.21)/Ni(0.58)]/Au(12) (b) and (d).

from an ideally flat surface) at the bottom Au/ML interface is $\sigma = \sigma^{\mathrm{Au/Co}} = 0.8$ nm, and at the top ML/Au interface $\sigma = \sigma^{\mathrm{Ni/Au}}$ is 1.6 nm for 16 ML and 1.8 nm for 32 ML. This analysis shows that both roughness and roughness period increase with the number N of ML. The increase in roughness period is clearly visible in the magnified cross-sectional STEM images of 16 and 32 ML in Figs. 5(c) and 5(d). We used the values of ξ and σ for $N = 0$ (the bottom ML interface), 16, and 32 to extrapolate ξ and σ for the rest of our MLs.

Table I summarizes the roughness, σ, and roughness period, ξ, of the Co/Ni MLs as a function of N. These values are used to analytically calculate K_{DIP} [Eq. (6)] and H_{DIP} [Eq. (11)], and numerically calculate K_{DIP}(calc) and H_{DIP}(calc).

Figure 6 shows the plots of K_S^{DIP}/d, K_S^{DIP}/d(calc), and $K_{S,r-f}^{\mathrm{DIP}}/d$(calc) as a function of N. We calculated $K_S^{\mathrm{DIP}}/d = (K_{S,T}^{\mathrm{DIP}} + K_{S,B}^{\mathrm{DIP}})/d$ by using Eq. (7) and assuming that the roughness of the top and bottom surfaces of the MLs are uncorrelated. K_S^{DIP}/d(calc) is numerically calculated assuming correlated roughness of the top and bottom film surfaces, and $K_{S,r-f}^{\mathrm{DIP}}/d$(calc) is numerically calculated assuming rough top and flat bottom film surfaces.

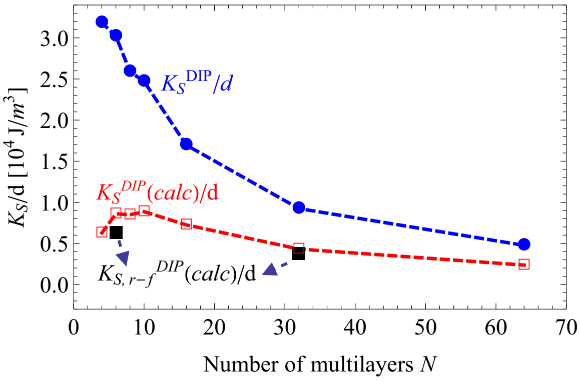

FIG. 6. Analytical [$K_S^{\mathrm{DIP}}/d = (K_{S,T}^{\mathrm{DIP}} + K_{S,B}^{\mathrm{DIP}})/d$] and numerical [$K_S^{\mathrm{DIP}}/d$(calc) and $K_{S,r-f}^{\mathrm{DIP}}/d$(calc)] calculations of the dipole surface anisotropy as a function of N. K_S^{DIP}/d is calculated from Eq. (7), and assuming that the roughness of the top and bottom surfaces of the ML are uncorrelated. K_S^{DIP}/d(calc) is calculated assuming correlated roughness of the top and bottom film surfaces, and $K_{S,r-f}^{\mathrm{DIP}}/d$(calc) is calculated assuming rough top and flat bottom film surfaces.

From Fig. 6 it is clear that K_S^{DIP}(calc) and $K_{S,r-f}^{\mathrm{DIP}}/d$(calc) are practically the same for $N = 32$ and comparable for $N = 6$. This indicates that the dipole surface anisotropy is similar if films have one rough and one flat surface or if they have two correlated rough surfaces. The calculations of K_S^{DIP}/d by using Eq. (7) take into account the roughness of the top and bottom surfaces. K_S^{DIP}/d for one flat and one rough surface is similar to the numerically calculated $K_{S,r-f}^{\mathrm{DIP}}/d$(calc) for thick films. This shows why K_S^{DIP}/d of films with uncorrelated rough surfaces is about two times larger than the numerically calculated K_S^{DIP}(calc) for films with two correlated film surfaces.

From Figs. 4 and 5 it is clear that the top and bottom surfaces of the Co/Ni MLs are correlated, even though the roughness period of the top surface increases slightly with N. Since K_S^{DIP}/d(calc) is determined assuming correlated top and bottom surfaces, we will use K_S^{DIP}/d(calc) to determine anisotropy, K_u, of our Co/Ni MLs.

3. *Magnetic properties of Co/Ni MLs*

M_s and K_u(SQUID) of the as-deposited Co/Ni MLs measured at 5 and 300 K by SQUID, and $K_2^{\perp}$, $K_4^{\perp}$, $K_u(\mathrm{FMR}) = K_2^{\perp} + K_4^{\perp}$, $g^{\perp}$, and $g^{\parallel}$ of the as-deposited Co/Ni MLs measured at 300 K by FMR are summarized in Table II. Additional plots of $\mu_0 M_{\mathrm{eff}}$ as a function of the number of multilayers, N, and g factor as a function of $1/N$ obtained from FMR measurements with the applied field in parallel and perpendicular direction to the sample surface are provided in the Supplemental Material [58].

TABLE II. N is the number of the Co/Ni MLs, and M_s and K_u(SQUID) are, respectively, the saturation magnetization and anisotropy of the as-deposited Co/Ni MLs measured by SQUID at 5 and 300 K. $K_2^{\perp}$, $K_4^{\perp}$, $K_u(\mathrm{FMR}) = K_2^{\perp} + K_4^{\perp}$ are anisotropy coefficients, and $g^{\perp}$ and $g^{\parallel}$ are g factors of the Co/Ni ML measured by FMR at 300 K. $K_4^{\perp}$ and $g^{\perp}$ of the Co/Ni ML with $N = 64$ are not determined since the perpendicular FMR measurements induce the spin wave oscillations in the ML. K_S^{DIP}/d(calc) and K_{DIP}(calc) listed in Table I are used to calculate K_u(SQUID) and K_u(FMR). For Co/Ni MLs with $N = 4$ and 6, the error bar in M_s is 12×10^{-3} A/m and the error bar in K_{SQUID} is 0.06 and 0.05 J/m^3, respectively.

	5 K		300 K							
N	M_s (10^3 A/m) $\pm$ 8	K_u(SQUID) (10^5 J/m^3) $\pm$ 0.03	M_s (10^3 A/m) $\pm$ 8	K_u(SQUID) $\pm$ 0.04	$K_2^{\perp}$(FMR) (10^5 J/m^3) $\pm$ 0.02	$K_4^{\perp}$(FMR) (10^5 J/m^3) $\pm$0.02	K_u(FMR) $\pm$0.04	$g^{\perp}$ $\pm$0.001	$g^{\parallel}$ $\pm$0.001	$g^{\perp} - g^{\parallel}$ $\pm$0.002
4	655	4.84	600	3.72	3.87	–0.23	3.64	2.206	2.197	0.009
6	710	5.31	686	4.23	4.53	–0.38	4.15	2.193	2.182	0.011
8	752	6.48	703	4.91	5.30	–0.39	4.91	2.187	2.173	0.014
10	789	7.11	759	5.62	5.99	–0.39	5.60	2.182	2.163	0.019
16	791	6.94	759	5.20	5.73	–0.37	5.36	2.177	2.161	0.016
32	782	6.67	759	4.89	5.45	–0.69	4.76	2.169	2.156	0.013
64	753	5.96	737	4.77	4.89					

Due to roughness the demagnetization field in the Co/Ni ML is lower than expected for ideally flat films. For this reason, the anisotropy coefficients in Table II are calculated using K_{DIP}(calc) listed in Table I: K_u(SQUID) is calculated by finding the area enclosed between the easy and hard axes M(H) curve and adding to this area K_{DIP}(calc). A plot of K_{eff} values determined from the enclosed area between the hard and easy axes M(H) curves at 5 and 298 K as a function of N is shown in the Supplemental Material [58]. K_u(FMR) is calculated from Eqs. (18).

$K_4^{\perp}$ and $g^{\perp}$ of the Co/Ni ML with $N = 64$ are not determined since we observed standing spin waves with the k vector perpendicular to the surface of the ML. The induced spin waves are possible due to the large thickness of this 64 ML that exceeds 50 nm.

Table II shows that the total anisotropy coefficients measured by FMR, K_u(FMR), are the same as those measured by SQUID, K_u(SQUID), at 300 K. For this reason in the analyses of K_u as a function of N we will only consider K_u(SQUID) values.

Figure 7 shows the M_s and K_u of Ta(3)/Au(12)/$N \times$ [Co(0.21)/Ni(0.58)]/Au(12) as a function of N measured at 5 and 300 K by SQUID. M_s increases with the increase in N and stays nearly constant for $N \geqslant 10$. The lower M_s for $N \leqslant 8$ is at least in part due to the interdiffusion of Au into the Co/Ni ML that was directly observed by the EDXS analyses in the TEM (Fig. 4).

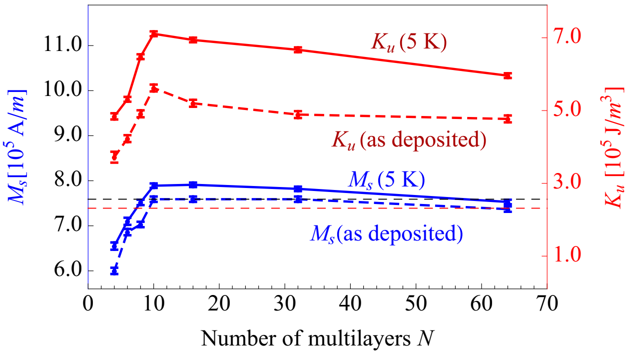

FIG. 7. The M_s and K_u of the as-deposited Co/Ni MLs as a function of the number of multilayers measured at 5 and 300 K. The dotted black and red lines represent M_s of Co/Ni MLs calculated assuming bulk M_s values for Co and Ni at 0 and 300 K, respectively.

K_u also increases sharply with N for $N \leqslant 10$ and then decreases with the further increase of N. A similar trend has already been observed by Qiu *et al.* [35] in Co$_{90}$Fe$_{10}$/Pt superlattice structures and Co/Ni ML by Sabino *et al.* [34]. At 300 K, M_s and K_u are reduced by approximately 5.7% and 29%, respectively, relative to their values at 5 K. The increase in K_u with temperature is nearly proportional to the increase in M_s^2 with temperature as expected from the mean-field theory. It is important to point out that the trends of both M_s and K_u do not change with the increase of temperature from 5 to 300 K, which indicates that they are not affected by thermal fluctuations. Thus, the drop of K_u for $N \leqslant 8$ is not due to the onset of superparamagnetism in ultrathin films.

FMR measurements show that both $g^{\perp}$ and $g^{\parallel}$ decrease with the increase of N, and that $g^{\perp}$ is larger than the $g^{\parallel}$ for all N's. The latter is in agreement with the results by Shaw *et al.* [50] for CoFe/Ni MLs grown on a Cu seed layer.

B. Annealed films

Structural and magnetic properties

The Au-Co and Au-Ni phase diagrams [62] depict no miscibility of Au into Co and a very small miscibility of Au into Ni below 523 K. For this reason we annealed the films at 523 and 553 K for 1 h in an attempt to expel the Au from the Co/Ni MLs. den Broeder *et al.* [57] observed the increase in the perpendicular to surface magnetic anisotropy of ion-beam sputtered Co/Au MLs after annealing at 523 and 553 K. They attributed the increase in PMA to the back diffusion of Au from Co layers.

In-plane and out-of-plane x-ray measurements were performed on all Co/Ni MLs after annealing at 523 K for 1 h. Figure 8 shows the distance between the lattice planes $d(111)$ (left axis) and $d(220)$ (right axis) of the annealed Co/Ni ML samples as a function of N. In comparison to the as-deposited

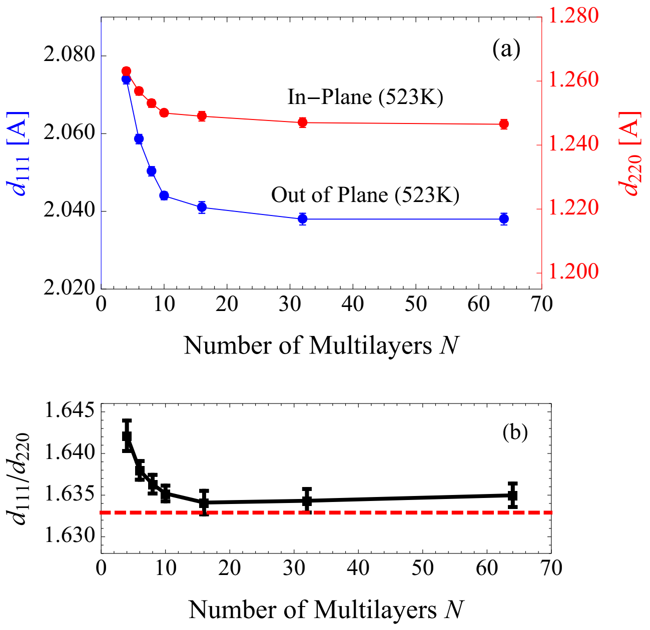

FIG. 8. (a) The spacing between the (111) and (220) lattice planes of the Co/Ni MLs annealed at 523 K as a function of N. (b) d_{111}/d_{220} of the annealed Co/Ni MLs as a function of N. The x-ray measurements are performed at room temperature.

samples, the spacing between both the lattice planes $d(111)$ and $d(220)$ slightly decreases after annealing [see Fig. 3(a)]. The reduction in the lattice volume due to annealing and in respect to the unstrained Co/Ni lattice is 9%. This supports the hypothesis that during the annealing process a small amount of Au leaves the crystal structure of the Co/Ni MLs.

The out-of-plane x-ray measurements also show an improvement in the texture of the Co/Ni MLs; the full width at half maximum of the rocking curve is reduced by 0.2°. This could result from grain growth and annihilation of the grains that do not grow along the ⟨111⟩ crystal orientations.

Figure 9 shows the M_s and K_u of the as-deposited and annealed (at 523 K) Co/Ni MLs as a function of the number of MLs. There is an increase of both M_s and K_u after annealing the ML samples. However, the increase in M_s and K_u is significantly larger for $N \leqslant 10$, where the concentration of Au is proportionally higher. This suggests that Au diffusion into the Co/Ni MLs causes at least in-part reduction of M_s. This may also indicate that Au diffusion into the Co/Ni MLs causes a reduction of K_u. As we will show in the next section this is due to an increase of the surface anisotropy at Au/ML and ML/Au interfaces after annealing.

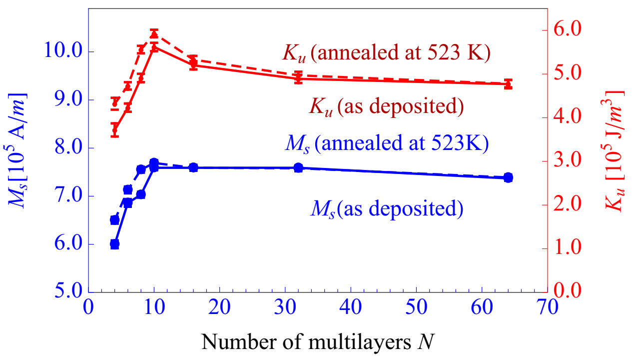

FIG. 9. The M_s and K_u of the as-deposited and annealed at 523 K Co/Ni MLs as a function of the number of MLs. The SQUID measurements are performed at room temperature.

An increase in the annealing temperature to 553 K leads to a drastic reduction in both M_s and K_u. Kurt *et al.* [30] also observed a reduction in K_u of the Co/Ni MLs grown on top of Au seed layers after annealing above 523 K. For the Co/Ni ML with $N = 8$, M_s decreases from 7.03×10^5 A/m to 4.81×10^5 A/m, and K_u decreases from 5.00×10^5 J/m^3 to 2.65×10^5 J/m^3. An intermixing of Co and Ni in the MLs could be responsible for the observed trend. Thus, annealing cannot be used to entirely remove Au from the Co/Ni MLs.

C. A simplified model including only surface anisotropies

In many reports [34–36,38,40,43,45] the change of the magnetic anisotropy in the ML structures as a function of ML thickness is analyzed by taking into account only the surface anisotropies. This simplified model can be expressed by using Eq. (2) (where K_{ME} and K_{MC} terms are ignored) and Eq. (12) as

$$K_u(\mathrm{calc}) = \frac{K_S}{d} = \frac{K_S^S}{d} + K_S^V$$
$$= \frac{\left(K_S^{\mathrm{Au/Co}} + K_S^{\mathrm{Ni/Au}} - K_S^{\mathrm{Co/Ni}}\right)}{d} + \frac{2K_S^{\mathrm{Co/Ni}}}{t_{\mathrm{BL}}}, \quad (19)$$

where $K_u(\mathrm{calc})$ is the calculated total intrinsic magnetic anisotropy of the ML. The first term, K_S^S, is inversely proportional to the ML thickness ($\propto 1/d$) and the second term, K_S^V, is independent of the ML thickness and only depends on the Co/Ni bilayer thickness, t_{BL}.

To separate K_S^S and K_S^V contributions, K_u(SQUID) of the as-deposited and annealed MLs (with $N = 4$, 6, 8, 10, 16, 32, and 64) is plotted as a function of $1/d$ in Fig. 10(a). K_u(SQUID) has linear dependence on $1/d$ for $N \geqslant 10$. From the linear fit of K_u(SQUID) with $1/d$ we obtain (a) (from intercepts) that $K_S^V = 2K_S^{\mathrm{Co/Ni}}/t_{\mathrm{BL}}$ is 4.58×10^5 J/m^3 for as-deposited and 4.54×10^5 J/m^3 for annealed ML, and (b) (from slopes) that $K_S^S = K_S^{\mathrm{Au/Co}} + K_S^{\mathrm{Ni/Au}} - K_S^{\mathrm{Co/Ni}}$ is 8.12×10^{-4} J/m^2 for as-deposited and 1.08×10^{-3} J/m^2 for annealed ML.

From the intercepts we calculate that $K_S^{\mathrm{Co/Ni}} = 1.83 \times 10^{-4}$ J/m^2 and $K_S^{\mathrm{Co/Ni}} = 1.82 \times 10^{-4}$ J/m^2 for the as-deposited and annealed ML, respectively, in agreement with the previously reported values [34,50] for $K_S^{\mathrm{Co/Ni}}$. Thus, it is evident that the bulk anisotropy, $2K_S^{\mathrm{Co/Ni}}/t_{\mathrm{BL}}$, is not affected by annealing.

From the slopes and the calculated value of $K_S^{\mathrm{Co/Ni}}$, we determined $K_S^{\mathrm{Au/Co}} + K_S^{\mathrm{Ni/Au}} = 0.99 \times 10^{-3}$ J/m^2 for as-deposited and $K_S^{\mathrm{Au/Co}} + K_S^{\mathrm{Ni/Au}} = 1.26 \times 10^{-3}$ J/m^2 for annealed ML, respectively. These values are twice as large as reported by other groups for Co/Au [55] and Ni/Au [63] superlattices. The reported values of $K_S^{\mathrm{Au/Co}}$ range from 3.7×10^{-4} J/m^2 to 5.8×10^{-4} J/m^2 and the reported value of $K_S^{\mathrm{Ni/Au}}$ is -1.5×10^{-4} J/m^2. For $N \geqslant 10$ the linear

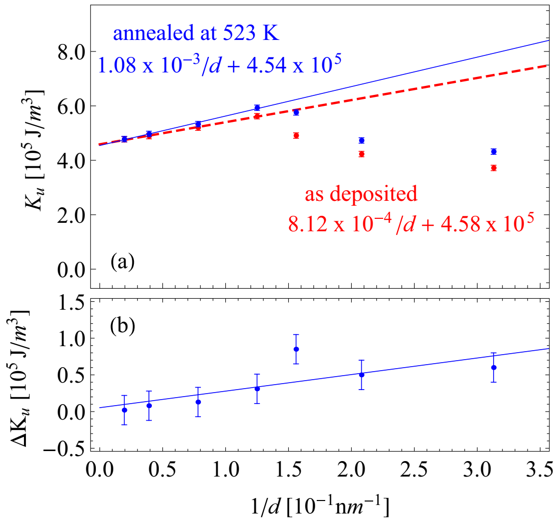

FIG. 10. (a) K_u(SQUID) as a function of $1/d$ for as-deposited and annealed at 523 K ML. The intercepts and slopes are obtained from a linear fit of the anisotropy coefficients for as-deposited (blue solid line) and annealed at 523 K (red dotted line) MLs. (b) $\Delta K_u = K_u(\text{annealed}) - K_u(\text{as-deposited})$ as a function of $1/d$. The solid blue line represents a linear fit of ΔK_u values.

dependence of K_u(SQUID) on $1/N$ is not only due to the surface anisotropy coefficients $K_S^{\text{Au/Co}} + K_S^{\text{Ni/Au}}$, since $g^{\perp} - g^{\parallel}$, which is proportional to K_{MC}, also scales with N. This could explain why this simplified analyses overestimate $K_S^{\text{Au/Co}} + K_S^{\text{Ni/Au}}$ in the ML.

Since annealing does not affect $K_S^{\text{Co/Ni}}$, the increase in slope ($K_S^{\text{Au/Co}} + K_S^{\text{Ni/Au}} - K_S^{\text{Co/Ni}}$) after annealing is due to the increase of $K_S^{\text{Au/Co}} + K_S^{\text{Ni/Au}}$. It is expected that after annealing Au/Co and Ni/Au interfaces become sharper due to the back diffusion of Au at these interfaces.

The difference between K_u of annealed and as-deposited Co/Ni MLs, $\Delta K_u = K_u(\text{annealed}) - K_u(\text{as-deposited})$, is plotted for all Co/Ni MLs in Fig. 10(b). The increase of K_u after annealing for all ML scales with $1/d$ indicating that the back diffusion of Au increases only the Au/ML and ML/Au surface anisotropies. From this we infer that the Au diffusion cannot explain the reduction of magnetic anisotropy for the Co/Ni MLs with $N < 10$.

The diffusion of Au in the Co/Ni MLs will introduce randomness in the magnetic pair bonding which will reduce magnetic anisotropy. On the other hand, Au is a large Z number element that may increase spin-orbit coupling in the Co/Ni ML that could lead to an increase of the magnetic anisotropy of the ML. Since $2K_S^{\text{Co/Ni}}/t_{\text{BL}}$ is not affected by annealing we will assume that these two contributions cancel out and the bulk magnetic energy will not change with diffusion of Au in the Co/Ni ML.

The simplified model that assumes only bulk and surface terms cannot explain the reduction of magnetic anisotropy of the Co/Ni MLs for $N < 10$ as evident from Fig. 10. For this reason, in the next section, a more complete model, which includes all anisotropy contributions discussed in the theory section, is used to describe the dependence of K_u(SQUID) on N.

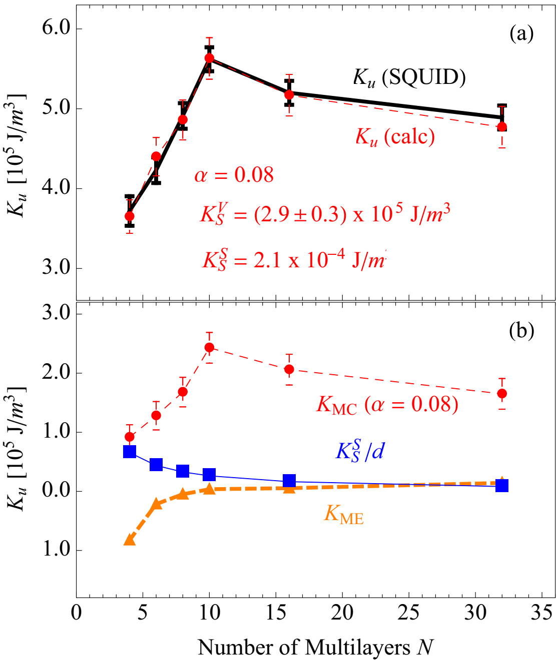

FIG. 11. (a) The SQUID measured magnetic anisotropy coefficients K_u(SQUID) (black line) and the calculated anisotropy coefficients $K_u(\text{calc}) = K_{\text{ME}} + K_{\text{MC}} + K_S^S/d + K_S^V$ (solid red circles). The values of α, K_S^S, and K_S^V are obtained from fitting K_u(SQUID) to the model. (b) Plots of K_{ME} (solid orange triangles), K_{MC} (solid red circles), and K_S^S/d (solid blue squares).

D. Models for magnetic anisotropy

In this section we will evaluate all anisotropy terms discussed in the theory section. In the proposed model the magnetic anisotropies measured by SQUID and FMR (Table II) are due to the magnetoelastic and magnetocrystalline energies in addition to the surface anisotropy discussed in the simplified model. From Eqs. (2) and (19) we can write

$$K_u(\text{calc}) = K_{\text{ME}} + K_{\text{MC}} + K_S^S/d + K_S^V. \tag{20}$$

In the model there are three fitting parameters: α in K_{MC}, surface anisotropy coefficient K_S^S, and K_S^V. The magnetic anisotropies K_{ME} and K_{MC} are calculated from Eq. (3) and Eq. (4), respectively.

Figure 11(a) shows the experimental K_u(SQUID) (solid black line) and the fit K_u(calc) (solid red circles) obtained using the model in Eq. (20) as a function of N. Figure 11(a) shows excellent agreement between the measurements and fit for all N values.

Figure 11(b) shows the individual contributions of anisotropy coefficients K_{ME} and K_{MC}, K_S^S, and K_S^V as a function of N. In Fig. 11(b) K_{ME} is practically 0 for $N \geqslant 10$. For $N < 10$, K_{ME} decreases with N and reaches -8.25×10^4 J/m^3 for $N = 4$. This is due to the expansion of $d(111)$ and $d(220)$ in the Co/Ni MLs observed for $N \leqslant 10$ [Fig. 3(a)]. Measured K_{ME} values are significantly larger than those reported for Co/Ni MLs grown on Au seed layers [4] and for CoFe/Ni MLs grown on Cu seed layers [50]. K_{MC} has the same dependence on N as K_u(SQUID); strongly increases with N for $N \leqslant 10$, and then decreases with further increase of N.

The model shows that for $N \leqslant 10$, the decrease in perpendicular magnetic anisotropy is predominantly due to K_{MC} and K_{ME}. A moderate decrease in perpendicular anisotropies for $N > 10$ is due to the reduction of K_{MC} and K_S^S.

From the fitting of experimental K_u(SQUID) data using Eq. (20), we find out that α in K_{MC} is 0.08, K_S^S is 2.1×10^{-4} J/m^2 and K_S^V is $2.9 \pm 0.3 \times 10^5$ J/m^3. The obtained value of α is in agreement with the results shown by Shaw *et al.* [50] ($\alpha = 0.097$) for the FeCo/Ni ML surrounded by Cu layers. From $K_S^V = 2K_S^{\mathrm{Co/Ni}}/t_{\mathrm{BL}}$ we found that $K_S^{\mathrm{Co/Ni}}$ is 1.2×10^{-4} J/m^2. This value is almost two times smaller than the previously reported $K_S^{\mathrm{Co/Ni}}$ [34,50].

The uniaxial orbital asymmetry at Co/Ni interfaces leads to an interface anisotropy $K_S^{\mathrm{Co/Ni}}$, and thus, the bulk anisotropy, K_S^V, the last term in Eq. (19). In addition this orbital asymmetry results in $g_\parallel < g_\perp$ as shown in Table II leading to uniaxial anisotropy K_{MC} [see Eq. (4)].

Our x-ray data analysis shows a tetragonal distortion of the lattice [see Fig. 3(b)]. This tetragonality can also lead to a uniaxial anisotropy. However, the tetragonal distortion does not follow the dependence of K_{MC} and K_S^V on N. In fact, the tetragonal distortion changes its sign for $N > 10$; is almost zero for $N = 10$, while $g_\perp - g_\parallel$ reaches maximum. It can only lead to a decrease in $g_\perp - g_\parallel$ for $4 < N < 10$ compared to that measured by FMR. K_S^V is independent of N and therefore has nothing to do with the tetragonal distortion. The tetragonal distortion therefore does not play any significant role in the measured uniaxial anisotropy.

Assuming that $K_S^{\mathrm{Co/Ni}} = 1.2 \times 10^{-4}$ J/m^2, $K_S^{\mathrm{Ni/Au}} = -1.5 \times 10^{-4}$ J/m^2, [63] and $K_S^S = K_S^{\mathrm{Au/Co}} + K_S^{\mathrm{Ni/Au}} - K_S^{\mathrm{Co/Ni}} = 2.1 \times 10^{-4}$ J/m^2 we can determine that $K_S^{\mathrm{Au/Co}} = 4.8 \times 10^{-4}$ J/m^2. This is in good agreement with reported values of $K_S^{\mathrm{Au/Co}}$ that range from 3.7×10^{-4} to 5.8×10^{-4} J/m^2 [55,63,64].

For simplicity, in the above discussion we neglected the surface magnetocrystalline anisotropies $\Delta K_S^{\mathrm{Au/Co}}$, $\Delta K_S^{\mathrm{Ni/Au}}$, and $\Delta K_S^{\mathrm{Co/Ni}}$ induced by the ML roughness. Using Eqs. (13)–(15) we can calculate that $\Delta K_S^{\mathrm{Au/Co}} = -3.4 \times 10^{-5}$ J/m^2, $\Delta K_S^{\mathrm{Ni/Au}}$ ranges from 1.6 to 2.1×10^{-5} J/m^2 for $N = 4$ and 32, respectively, and $\Delta K_S^{\mathrm{Co/Ni}}$ ranges from -1.2 to -1.4 $\times 10^{-5}$ J/m^2 for $N = 4$ and 32, respectively. The variation in $\Delta K_S^{\mathrm{Ni/Au}}$ and $\Delta K_S^{\mathrm{Co/Ni}}$ is due to the fact that σ and ξ change with thickness. In the calculations we assumed that $K_S^{\mathrm{Au/Co}} = 4.8 \times 10^{-4}$ J/m^2, $K_S^{\mathrm{Ni/Au}} = -1.5 \times 10^{-4}$ J/m^2, and $K_S^{\mathrm{Co/Ni}} = 1.2 \times 10^{-4}$. It is evident that the surface magnetocrystalline anisotropies (ΔK_S) are an order of magnitude lower than the surface anisotropies (K_S). Adding ΔK_S in the model [Eq. (20)] will not change the values of fitted parameters α, K_S^S, and K_S^V. However, the surface anisotropies $K_S^{\mathrm{Au/Co}}$, $K_S^{\mathrm{Ni/Au}}$, and $K_S^{\mathrm{Co/Ni}}$ will be about 10% larger since in this case $K_S^S = K_S^{\mathrm{Au/Co}} + \Delta K_S^{\mathrm{Au/Co}} + K_S^{\mathrm{Ni/Au}} + \Delta K_S^{\mathrm{Ni/Au}} - K_S^{\mathrm{Co/Ni}} - \Delta K_S^{\mathrm{Co/Ni}}$ and $K_S^V = 2(K_S^{\mathrm{Co/Ni}} + \Delta K_S^{\mathrm{Co/Ni}})/t_{\mathrm{BL}}$ ($\Delta K_S^{\mathrm{Ni/Au}}, \Delta K_S^{\mathrm{Au/Co}}$ and $\Delta K_S^{\mathrm{Co/Ni}}$ have negative values).

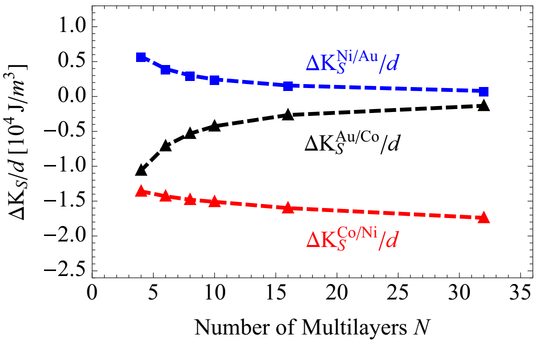

FIG. 12. Plot of $\Delta K_S^{\mathrm{Au/Co}}/d$, $\Delta K_S^{\mathrm{Ni/Au}}/d$, and $\Delta K_S^{\mathrm{Co/Ni}}/d$ as a function of N.

$\Delta K_S^{\mathrm{Au/Co}}/d$, $\Delta K_S^{\mathrm{Ni/Au}}/d$, and $\Delta K_S^{\mathrm{Co/Ni}}/d$ are plotted as a function of N in Fig. 12. Figure 12 shows that $\Delta K_S^{\mathrm{Au/Co}}$ and $\Delta K_S^{\mathrm{Ni/Au}}$ have $1/d$ dependence, while $\Delta K_S^{\mathrm{Co/Ni}}$ is practically independent of the ML thickness. Co/Ni interfaces are uniformly distributed throughout the ML and the variation of $\Delta K_S^{\mathrm{Co/Ni}}$ with d is only due to the change of roughness across the ML thickness.

V. CONCLUSION

The change in magnetic anisotropy of (111) textured Au/$N \times$ [Co/Ni]/Au films is studied as a function of the number of bilayer repeats N ($N = 4$, 6, 8, 10, 16, 32, and 64). The ferromagnetic resonance and SQUID measurements show that the perpendicular magnetic anisotropy of as-deposited and annealed Co/Ni multilayers first increases with N ($N \leqslant 10$) and then moderately decreases with $N > 10$, reaching the maximum value $K_u = 5.71 \times 10^5$ J/m^3 for $N = 10$.

The SQUID measurements show that the trends of both M_s and K_u do not change with increase of temperature from 5 to 300 K. This indicates that the reduction in the magnetic anisotropy for $N \leqslant 10$ is not due to the onset of the superparamagnetism in ultrathin films.

The in-plane and out-of-plane ferromagnetic resonance measurements show that the difference between the perpendicular and parallel g factors of Co/Ni multilayers has the same dependence on N as the experimentally measured magnetic anisotropies.

The lattice mismatch between Co and Ni, and Au (about 14%) induces a large strain in the films. In-plane and out-of-plane x-ray measurements show the expansion of the lattice spacing between orthogonal (220) and (111) planes of Co/Ni multilayers. EDXS analysis in TEM confirms the diffusion of Au into the Co/Ni multilayers that could be responsible for the observed expansion of the lattice volume in the multilayers. The strain calculations from x-ray measurements show that, with the change in N from 4 to 64, the magnetoelastic coefficient changes from -8.25×10^4 J/m^3 to 1.21×10^4 J/m^3. The diffusion of Au into the Co/Ni ML also causes reduction of M_s.

The cross-sectional STEM reveals that the roughness and roughness period increase with the number of the Co/Ni ML. The roughness causes up to a 3.5% decrease in the dipolar anisotropy of the ML. It also causes up to a 10% reduction in the surface magnetocrystalline anisotropy of the ML.

Annealing triggers partial back diffusion of Au from the ML. This results in an increase of only surface anisotropy while the bulk anisotropy stays unchanged.

The experimentally obtained dependence of the magnetic anisotropy of the Co/Ni ML on N is successfully modeled assuming contributions from the surface anisotropy, the magnetocrystalline anisotropy arising from the difference between the perpendicular and parallel g factors, and the magnetoelastic anisotropy due to the strain. The models reveal the strong decrease of the perpendicular magnetic anisotropy for $N < 10$ is predominantly due to the reduction in the magnetocrystalline and magnetoelastic anisotropies. On the other hand, a moderate decrease in the perpendicular magnetic anisotropy for $N > 10$ is due to the reduction in the magnetocrystalline anisotropy and the surface anisotropy between Au and the ML.

ACKNOWLEDGMENTS

Financial support for this project was provided by the Natural Sciences and Engineering Research Council of Canada (NSERC). The use of HZDR Ion Beam Centre TEM facilities and the support by its staff is gratefully acknowledged. In particular, we acknowledge the funding of TEM Talos by the German Federal Ministry of Education of Research (BMBF) under Grant No. 03SF0451 in the framework of HEMCP.

[1] F. Gimbert, L. Calmels, and S. Andrieu, Phys. Rev. B **84**, 094432 (2011).

[2] S. Girod, M. Gottwald, S. Andrieu, S. Mangin, J. McCord, E. E. Fullerton, J.-M. L. Beaujour, B. J. Krishnatreya, and A. D. Kent, Appl. Phys. Lett. **94**, 262504 (2009).

[3] G. H. O. Daalderop, P. J. Kelly, and F. J. A. den Broeder, Phys. Rev. Lett. **68**, 682 (1992).

[4] M. Gottwald, S. Andrieu, F. Gimbert, E. Shipton, L. Calmels, C. Magen, E. Snoeck, M. Liberati, T. Hauet, E. Arenholz, S. Mangin, and E. E. Fullerton, Phys. Rev. B **86**, 014425 (2012).

[5] M. Gottwald, S. Girod, S. Andrieu, and S. Mangin, IOP Conf. Ser.: Mater. Sci. Eng. **12**, 012018 (2010).

[6] J.-M. Beaujour, W. Chen, K. Krycka, C.-C. Kao, J. Z. Sun, and A. D. Kent, Eur. Phys. J. B **59**, 475 (2007).

[7] S. Mangin, D. Ravelosona, J. A. Katine, M. J. Carey, B. D. Terris, and E. E. Fullerton, Nat. Mater. **5**, 210 (2006).

[8] H.-S. Song, K.-D. Lee, J.-W. Sohn, S.-H. Yang, S. S. P. Parkin, C.-Y. You, and S.-C. Shin, Appl. Phys. Lett. **102**, 102401 (2013).

[9] J. M. Shaw, H. T. Nembach, and T. J. Silva, J. Appl. Phys. **108**, 093922 (2010).

[10] T. Kato, Y. Matsumoto, S. Kashima, S. Okamoto, N. Kikuchi, S. Iwata, O. Kitakami, and S. Tsunashima, IEEE Trans. Magn. **48**, 3288 (2012).

[11] S. Kaka, M. R. Pufall, W. H. Rippard, T. J. Silva, S. E. Russek, J. A. Katine, and M. Carey, J. Magn. Magn. Mater. **286**, 375 (2005).

[12] S. Kaka, M. R. Pufall, W. H. Rippard, T. J. Silva, S. E. Russek, and J. A. Katine, Nature (London) **437**, 389 (2005).

[13] O. Hellwig, T. Hauet, T. Thomson, E. Dobisz, J. D. Risner-Jamtgaard, D. Yaney, B. D. Terris, and E. E. Fullerton, Appl. Phys. Lett. **95**, 232505 (2009).

[14] T. Hauet, E. Dobisz, S. Florez, J. Park, B. Lengsfield, B. D. Terris, and O. Hellwig, Appl. Phys. Lett. **95**, 262504 (2009).

[15] M. Ranjbar, S. N. Piramanayagam, S. K. Wong, R. Sbiaa, and T. C. Chong, Appl. Phys. Lett. **99**, 142503 (2011).

[16] B. D. Terris and T. Thomson, J. Phys. D **38**, R199 (2005).

[17] M. E. Schabes, J. Magn. Magn. Mater. **320**, 2880 (2008).

[18] H. J. Richter, A. Y. Dobin, R. T. Lynch, D. Weller, R. M. Brockie, O. Heinonen, K. Z. Gao, J. Xue, R. J. M. V. D. Veerdonk, P. Asselin, and M. F. Erden, Appl. Phys. Lett. **88**, 222512 (2006).

[19] K. Kyuno, J.-G. Ha, R. Yamamoto, and S. Asano, Jpn. J. Appl. Phys. **35**, 2774 (1996).

[20] M. T. Johnson, J. J. de Vries, N. W. E. McGee, J. aan de Stegge, and F. J. A. den Broeder, Phys. Rev. Lett. **69**, 3575 (1992).

[21] D. Sander, J. Phys.: Condens. Matter **16**, R603 (2004).

[22] O. Hjortstam, K. Baberschke, J. M. Wills, B. Johansson, and O. Eriksson, Phys. Rev. B **55**, 15026 (1997).

[23] M. Sakamaki, K. Amemiya, M. O. Liedke, J. Fassbender, P. Mazalski, I. Sveklo, and A. Maziewski, Phys. Rev. B **86**, 024418 (2012).

[24] C.-R. Chang, Phys. Rev. B **48**, 15817 (1993).

[25] M. Johnson, F. den Broeder, J. de Vries, N. McGee, R. Jungblut, and J. aan de Stegge, J. Magn. Magn. Mater. **121**, 494 (1993).

[26] F. Gimbert and L. Calmels, Phys. Rev. B **86**, 184407 (2012).

[27] Y. Zhang, J. Woollam, Z. Shan, J. Shen, and D. Sellmyer, IEEE Trans. Magn. **30**, 4440 (1994).

[28] F. den Broeder, E. Janssen, W. Hoving, and W. Zeper, IEEE Trans. Magn. **28**, 2760 (1992).

[29] V. M. Naik, S. Hameed, R. Naik, L. Pust, L. E. Wenger, G. L. Dunifer, and G. W. Auner, J. Appl. Phys. **84**, 3273 (1998).

[30] H. Kurt, M. Venkatesan, and J. M. D. Coey, J. Appl. Phys. **108**, 073916 (2010).

[31] Y. Zhang and J. Woollam, IEEE Trans. Magn. **31**, 3262 (1995).

[32] E. Yang, V. M. Sokalski, M. T. Moneck, D. M. Bromberg, and J.-G. Zhu, J. Appl. Phys. **113**, 17C116 (2013).

[33] D. Stanescu, D. Ravelosona, V. Mathet, C. Chappert, Y. Samson, C. Beigne, N. Vernier, J. Ferre, J. Gierak, E. Bouhris, and E. E. Fullerton, J. Appl. Phys. **103**, 07B529 (2008).

[34] M. P. R. Sabino, M. Tran, C. Hin Sim, Y. Ji Feng, and K. Eason, J. Appl. Phys. **115**, 17C512 (2014).

[35] J. Qiu, Z. Meng, Y. Yang, J. F. Ying, Q. J. Yap, and G. Han, AIP Adv. **6**, 056123 (2016).

[36] P. J. H. Bloemen, W. J. M. D. Jonge, and F. J. A. D. Broeder, J. Appl. Phys. **72**, 4840 (1992).

[37] A. Rozatian, B. Fulthorpe, T. Hase, D. Read, G. Ashcroft, D. Joyce, P. Grundy, J. Amighian, and B. Tanner, J. Magn. Magn. Mater. **256**, 365 (2003).

[38] M. Suzuki, K. Kudo, K. Kojima, T. Yasue, N. Akutsu, W. A. Diño, H. Kasai, E. Bauer, and T. Koshikawa, J. Phys.: Condens. Matter **25**, 406001 (2013).

[39] L. You, R. C. Sousa, S. Bandiera, B. Rodmacq, and B. Dieny, Appl. Phys. Lett. **100**, 172411 (2012).

[40] S. T. Lim, M. Tran, J. W. Chenchen, J. F. Ying, and G. Han, J. Appl. Phys. **117**, 17A731 (2015).

[41] A. Barman, S. Wang, O. Hellwig, A. Berger, E. E. Fullerton, and H. Schmidt, J. Appl. Phys. **101**, 09D102 (2007).

[42] E. H. M. van der Heijden, K. J. Lee, Y. H. Choi, T. W. Kim, H. J. M. Swagten, C.-Y. You, and M. H. Jung, Appl. Phys. Lett. **102**, 102410 (2013).

[43] A. S. H. Rozatian, C. H. Marrows, T. P. A. Hase, and B. K. Tanner, J. Phys.: Condens. Matter **17**, 3759 (2005).

[44] S. Mizukami, X. Zhang, T. Kubota, H. Naganuma, M. Oogane, Y. Ando, and T. Miyazaki, Appl. Phys. Express **4**, 013005 (2011).

[45] M. Haertinger, C. H. Back, S.-H. Yang, S. S. P. Parkin, and G. Woltersdorf, J. Phys. D **46**, 175001 (2013).

[46] D. R. Linde, *CRC Handbook of Chemistry and Physics*, 84th ed. (CRC Press LLC, Boca Raton, FL, 2004), pp. 12–19.

[47] J. Huang, T. Wang, C. Yu, Y. Hu, P. Lee, and M. Yang, J. Cryst. Growth **171**, 442 (1997).

[48] D. Sander, Rep. Prog. Phys. **62**, 809 (1999).

[49] P. Bruno, Phys. Rev. B **39**, 865 (1989).

[50] J. M. Shaw, H. T. Nembach, and T. J. Silva, Phys. Rev. B **87**, 054416 (2013).

[51] J. M. Shaw, H. T. Nembach, and T. J. Silva, Phys. Rev. B **85**, 054412 (2012).

[52] P. Bruno, J. Appl. Phys. **64**, 3153 (1988).

[53] D. Süß, T. Schrefl, J. Fidler, and J. Chapman, J. Magn. Magn. Mater. **196-197**, 617 (1999).

[54] P. Bruno, J. Phys. F **18**, 1291 (1988).

[55] M. T. Johnson, P. J. H. Bloemen, F. J. A. den Broeder, and J. J. D. Vries, Rep. Prog. Phys. **59**, 1409 (1996).

[56] H. J. G. Draaisma and W. J. M. de Jonge, J. Appl. Phys. **64**, 3610 (1988).

[57] F. J. A. den Broeder, D. Kuiper, A. P. van de Mosselaer, and W. Hoving, Phys. Rev. Lett. **60**, 2769 (1988).

[58] See Supplemental Material at http://link.aps.org/supplemental/10.1103/PhysRevB.96.024401 for further information on M(H) curves obtained from SQUID measurements, resonance field versus frequency plots obtained from FMR measurements, and further information of effective anisotropy and g factors calculated from FMR measurements.

[59] E. Montoya, T. McKinnon, A. Zamani, E. Girt, and B. Heinrich, J. Magn. Magn. Mater. **356**, 12 (2014).

[60] E. Montoya, T. Sebastian, H. Schultheiss, B. Heinrich, R. E. Camley, and Z. Celinski, in *Magnetism of Surfaces, Interfaces, and Nanoscale Materials*, 1st ed., edited by R. E. Camley, Z. Celinski, and R. L. Stamps (Elsevier Science, Amsterdam, 2016), Vol. 5, pp. 113–167.

[61] M. Henini, *Molecular Beam Epitaxy, From Research to Mass Production*, 1st ed. (Elsevier Science, Amsterdam, 2012), p. 456.

[62] B. C. Giessen, *Developments in the Structural Chemistry of Alloy Phases* (Plenum, New York, 1969).

[63] J. R. Childress, C. L. Chien, and A. F. Jankowski, Phys. Rev. B **45**, 2855 (1992).

[64] C. Chappert, K. L. Dang, P. Beauvillain, H. Hurdequint, and D. Renard, Phys. Rev. B **34**, 3192 (1986).